

Giant Memcapacitance in Topotactic Redox Interfaces

W. R. Acevedo^{1,2}, C. A. M. van den Bosch³, M. H. Aguirre^{4,5,6}, C. Acha^{2,7}, A. Cavallaro³, C. Ferreyra^{1,2}, M. J. Sánchez^{2,8}, L. Patrone⁹, A. Aguadero^{3,*}, D. Rubi^{1,2}

¹ *Comisión Nacional de Energía Atómica and Instituto de Nanociencia y Nanotecnología, Centro Atómico Constituyentes, 1650, Buenos Aires, Argentina*

² *Consejo Nacional de Investigaciones Científicas y Técnicas, Godoy Cruz 2290 (1425), Buenos Aires, Argentina.*

³ *Department of Materials, Imperial College London, London, SW7 2AZ, United Kingdom*

⁴ *Departamento de Física de Materia Condensada, Universidad de Zaragoza, Pedro Cerbuna 12 50009 Zaragoza - Spain*

⁵ *Laboratorio de Microscopías Avanzada (LMA), Instituto de Nanociencia de Aragón (INA)-Universidad de Zaragoza, C/Mariano Esquillor s/n. 50018 Zaragoza, Spain*

⁶ *Instituto de Ciencias de Materiales de Aragón (ICMA), Universidad de Zaragoza, Zaragoza, Spain*

⁷ *Depto. de Física, FCEyN, Universidad de Buenos Aires & IFIBA-CONICET, Pab I, Ciudad Universitaria, Buenos Aires (1428), Argentina*

⁸ *INN, Centro Atómico Bariloche and Instituto Balseiro, 8400 San Carlos de Bariloche, Argentina*

⁹ *INTI, CMNB, Av. Gral Paz 5445, B1650KNA San Martín, Buenos Aires, Argentina*

The possibility to develop neuromorphic computing devices able to mimic the extraordinary data processing capabilities of biological systems spurs the research on memristive systems. Memristors with additional functionalities such as robust memcapacitance can outperform standard memristive devices in key aspects such as power consumption or miniaturization possibilities. In this work, we demonstrate a giant memcapacitive response of a perovskite memristive nanostructured interface, using the topotactic redox ability of $\text{La}_{0.5}\text{Sr}_{0.5}\text{Mn}_{0.5}\text{Co}_{0.5}\text{O}_{3-\delta}$ (LSMCO, $0 \leq \delta \leq 0.62$). We demonstrate that after an electroforming process that modifies the LSMCO nanostructure and creates channels for easy oxygen migration in and out of the device, the multi-mem behaviour originates at the switchable n-p diode formed at the Nb:SrTiO₃/LSMCO interface, where the acceptors/donors balance is dramatically changed upon electrically induced LSMCO oxidation and reduction. We found a memcapacitive effect $C_{\text{HIGH}}/C_{\text{LOW}} \sim 10^4$ for the interface and > 300 for the complete Nb:SrTiO₃/LSMCO/Pt device, which is the largest figure measured to date by at least a factor of 30. Our work opens a promising venue to design topotactic redox materials for disruptive nanoelectronic devices, with straightforward applications in neuromorphic computing technology.

* Corresponding author: a.aguadero@imperial.ac.uk (AA)

1. Introduction

Neuromorphic computing devices aim to mimic biological systems and are expected to dramatically improve performance and efficiency of electronic devices, enabling the development of advanced information technology including complex data analysis and pattern recognition.^[1] Brain synapses can be emulated by memristors,^[2,3] consisting of capacitor-like structures which display a reversible and non-volatile electrical resistance change upon the application of electrical stimulus.^[4,5] Other potential applications of memristors include nanoelectronic memories^[2] and logic gates.^[6] Memristive behavior is ubiquitously found in transition metal oxides, including perovskite manganites.^[7] Proposed memristive mechanisms for metal/manganite systems include the modulation of metal/insulator Schottky barriers due to oxygen vacancies drift-diffusion,^[8-10] or the interfacial redox reaction occurring when a reactive electrode (Ti or Al) is used.^[11-13] In the former case, the movement of a small number of oxygen vacancies *within* the manganite is usually assumed, and oxygen exchange with the environment is neglected.^[9] Alternatively, a robust memristive effect can be anticipated for perovskites displaying topotactic redox ability, i.e. the capability of reversibly storing and releasing oxygen without structural change.^[14,15] In this case, the memristive effect would rely on the electrical switch between oxidized and reduced phases with different electrical conductivities.^[16] In this scenario, significant exchange of oxygen with the surrounding atmosphere can be expected.

On the other hand, memcapacitance –that is the non-volatile change of a device capacitance C upon the application of electrical stress- is an additional functionality of memristors that has scarcely been explored.^[17-23] Proposed mechanisms are related to the creation and annihilation of conducting nanofilaments,^[17,18] the modulation of the Schottky barrier at metal/insulator interfaces,^[18,19] the electrical bias-induced redox of a TiO_x active layer^[20] or changes in the oxide permittivity upon oxygen vacancies electromigration.^[21,22] While applications for memcapacitance, including neuromorphic computing devices, have been proposed (see^[24] and references therein), the interest in this phenomenon has been hampered by the small reported figures to date ($C_{\text{HIGH}}/C_{\text{LOW}} \leq 10$).^[17-23] For instance, Nielen *et al.* reported that associated capacitive networks, suitable for efficient pattern recognition, can be build from cells able to switch their capacitance between C_{HIGH} and C_{LOW} , where the array size –linked to the device computing capability- scales with $C_{\text{HIGH}}/C_{\text{LOW}}$ ratio.^[25] This evidences the high technological interest of novel memcapacitive systems with large response.

In this paper we show that the nanostructured interface between the perovskite manganite with topotactic redox ability $\text{La}_{0.5}\text{Sr}_{0.5}\text{Mn}_{0.5}\text{Co}_{0.5}\text{O}_{3-\delta}$ (LSMCO, $0 \leq \delta \leq 0.62$, p-type)^[15] and $\text{Nb}:\text{SrTiO}_3$ (NSTO, 0.05 wt%, n-type) behaves as a switchable n-p diode with memristive and giant

memcapacitive behavior. Memcapacitance figures are $C_{HIGH}/C_{LOW} \sim 10^4$ for the NSTO/LSMCO interface and > 300 for the complete NSTO/LSMCO/Pt device. We show that after an electroforming process that modifies the LSMCO nanostructure and creates channels for easy oxygen migration, the observed multi-mem behavior is related to the electrical switch between LSMCO oxidized and reduced phases. This allows large changes in the donor/acceptor balance at the NSTO/LSMCO interface, tuning the diode depletion layer. The phenomena reported here opens a new pathway for the development of novel neuromorphic computing devices based on topotactic redox materials and multi-mem interfaces.

2. Experimental

Oxidized phase LSMCO thin films were grown by pulsed laser deposition (PLD) on Nb:SrTiO₃ (0.5 wt%, 001) single crystals from CrysTec GmbH Kristalltechnologie, using a KrF excimer laser with $\lambda = 248\text{nm}$. The growth temperature, oxygen pressure and laser fluence were fixed at 800°C, 0.04 mbar and 0.5 – 1J/cm² respectively. After deposition, the oxygen pressure was increased to 800mbar while the films were cooled at 10°C/min. Pristine LSMCO film thicknesses were extracted from X-ray reflectivity (see Supplementary Information, Figure S1(a)) and from STEM-HAADF images and were in the range 17 – 20nm. X-ray diffraction characterization was performed with a PANalytical X'Pert Pro MRD diffractometer ($\lambda = 1.5418\text{\AA}$), an X'Celerator detector and a 4-angle goniometer with a crystal monochromator. The presence of epitaxial growth is evidenced from Bragg-Brentano scans, as shown in the Supplementary Information Figure S1(b). Reciprocal space maps indicate that the films are fully strained (see Supplementary Information, Figure S2). Atomic force microscopy (AFM) images were recorded with an Asylum Research MFP 3D microscope with PPP-NCHR tips from Windsor Scientific, with typical root mean square roughness $\sim 2.7\text{nm}$. Representative morphologies are displayed in the Supplementary Information, Figure S3. Top Pt electrodes, $\sim 20\text{nm}$ thick, were deposited by sputtering and microstructured by either FIB or optical lithography. A Dual Beam Helios 650 was used to acquire scanning electron microscopy images and prepare FIB lamellas to observe cross-sections. High resolution scanning transmission electron microscopy was performed using a FEI Titan G2 microscope at 300 kV with probe corrector and *in situ* EELS spectrum acquisition with a Gatan Energy Filter Tridiem 866 ERS. Electrical characterization was performed at room temperature with a Keithley 2612 source-meter connected to a Suss probe station with a thermal holder. The NSTO substrate was grounded and used as the bottom electrode. A drop of silver paint (area $\sim 1\text{mm}^2$) was deposited on the side of the NSTO substrate to make electrical contact. The electrical stimulus was applied to the top Pt electrode. Dynamic I-V curves were obtained by applying a sequence of voltage pulses of different amplitudes ($0 \rightarrow V_{MAX} \rightarrow V_{MIN} \rightarrow 0$, with a time-width of 1ms and a step of

100mV), with the current measured during the application of the pulse. Additionally, after each voltage pulse a small reading voltage was applied to allow the current to be measured and the remnant resistance state determined, obtaining the so-called hysteresis switching loops (HSLs). Complex impedance was measured using an AutoLab PGSTAT302N impedance analyzer at room temperature. A fixed AC signal of 100mV was applied, with frequencies between 10Hz and 1MHz. Dynamic capacitance-voltage (C-V) curves were obtained using a standard LCR meter by assuming a CR parallel circuit. DC voltage pulses of increasing amplitude were applied with a small superimposed AC signal (10kHz, amplitude 200mV) to extract the dynamic capacitance of the device. Between each of these pulses, a pure AC signal was applied to obtain the remnant capacitance value.

3. Results and Discussion

3.1. Electroforming process and memristive behavior

Electrical characterization was performed on NSTO/LSMCO/Pt devices. Platinum was selected as the top electrode due to its high work function (5.6eV) which, in contact with the p-type LSMCO, gives a quasi-ohmic interface.^[26] The virgin resistances of $37.5 \times 10^3 \mu\text{m}^2$ NSTO/LSMCO/Pt devices were $\sim 1\text{M}\Omega$, and the current-voltage (I-V) curves for low stimulus, shown in Figure 1(a), display a rectifying behavior linked to the formation of an n-p diode at the NSTO / LSMCO interface. The inset of Figure 1(b) shows that the forming process is triggered when a -7V pulse is applied, resulting in a sudden resistance drop to $\sim 50\Omega$. After forming, dynamic I-V curves and hysteresis switching loops (HSL) both demonstrate the memristive properties of our devices, as shown in Figures 1(b) and 1(c). The device switches from a low resistance state (R_{LOW}) to a high resistive state (R_{HIGH}) (RESET process) upon the application of $\sim +5.5\text{V}$, while the opposite behavior (SET process) is observed upon the application of $\sim -1.5\text{V}$. From the second cycle, R_{HIGH} and R_{LOW} stabilize to $\sim 1\text{-}2\text{k}\Omega$ and $\sim 100\text{-}300\Omega$, respectively, giving an ON/OFF ratio of ~ 10 . Figure 2(a) shows retentivities of at least 10^4s for both resistive states, while Figure 2(b) shows an endurance test with a stable behavior for 220 cycles.

Figure 1(d) shows that a “bubble” is formed at the Pt top electrode upon forming, and three distinct zones are identified. Zone 1 has a diameter of $\sim 5\mu\text{m}$ and corresponds to the contact position of the tip. Zone 2 is a ring of higher contrast than Zone 1 (d: $\sim 15\mu\text{m}$) where some material from the film and the Pt electrode has been expelled during the forming process. Zone 3 displays similar contrast to Zone 1. Formation of a “bubble” is usually linked to O_2 gas release upon electroforming,^[27] and suggests that the LSMCO memristive behavior is related to its

topotactic redox ability where oxidation (reduction) of the LSMCO lattice is associated with the SET (RESET) process and produces a low (high) resistance state.

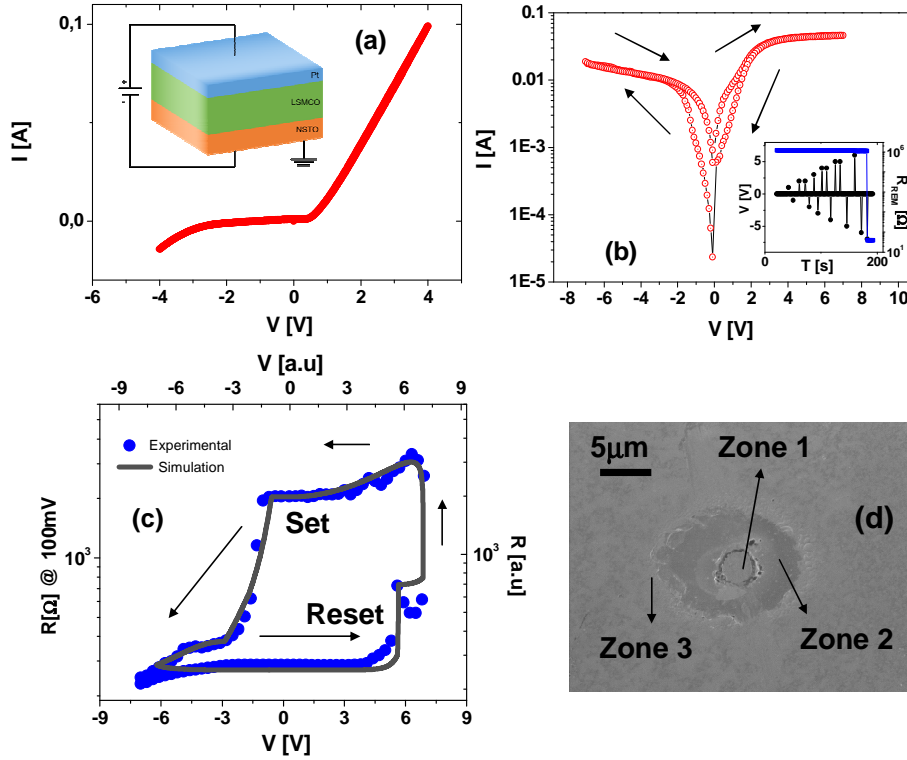


Figure 1: (a) Representative low-stimuli current-voltage (I-V) curve recorded on a pristine NSTO/LSMCO/Pt device. Rectifying behavior is evident, linked to the existence of an n-p diode at the NSTO/LSMCO interface. Inset shows a sketch of the device electrical connection. (b) Dynamic pulsed I-V curve recorded on an electroformed device with arrows indicating the circulation direction of the curve ($0 \rightarrow 7V \rightarrow -7V \rightarrow 0$, with a time-width of 1ms and a step of 100mV). The presence of hysteresis is a signature of memristive behavior. Inset shows that the electroforming process occurs after the application of a -7V pulse. (c) Experimental hysteresis switching loop (HSL, remanent resistance vs. applied voltage curve, in solid circles), recorded simultaneously with the dynamic I-V curve, displaying the presence of two well defined non-volatile resistance states. The corresponding simulated HSL is displayed with a solid line. (d) Scanning electron microscopy image (top-view) of a formed device. Three zones are identified and described in the text.

This scenario is supported by experiments performed in vacuum ($<1 \times 10^{-2}$ mbar) and displayed in Figure 2(c). It is found that the forming process in vacuum follows the application of a -7V pulse. After forming, voltage ramps were applied (starting with positive voltage) and the first RESET event is triggered at $\sim +5.5V$. For both the forming and first RESET processes, the voltages correspond with those found for devices in an air atmosphere. However, upon further

stimulus with negative voltage, the SET process, observed at $\sim -1.5\text{V}$ in air atmosphere, does not occur in vacuum, providing evidence that environmental O_2 is critical for setting the device to R_{LOW} state through LSMCO oxidation. Figure 2(d) displays the normalized temperature dependence of both R_{HIGH} and R_{LOW} in air, showing a thermally activated semiconducting-like behavior in both cases, resembling the measurements performed on bulk oxidized and reduced LSMCO phases (see Suppl. Figure S4).

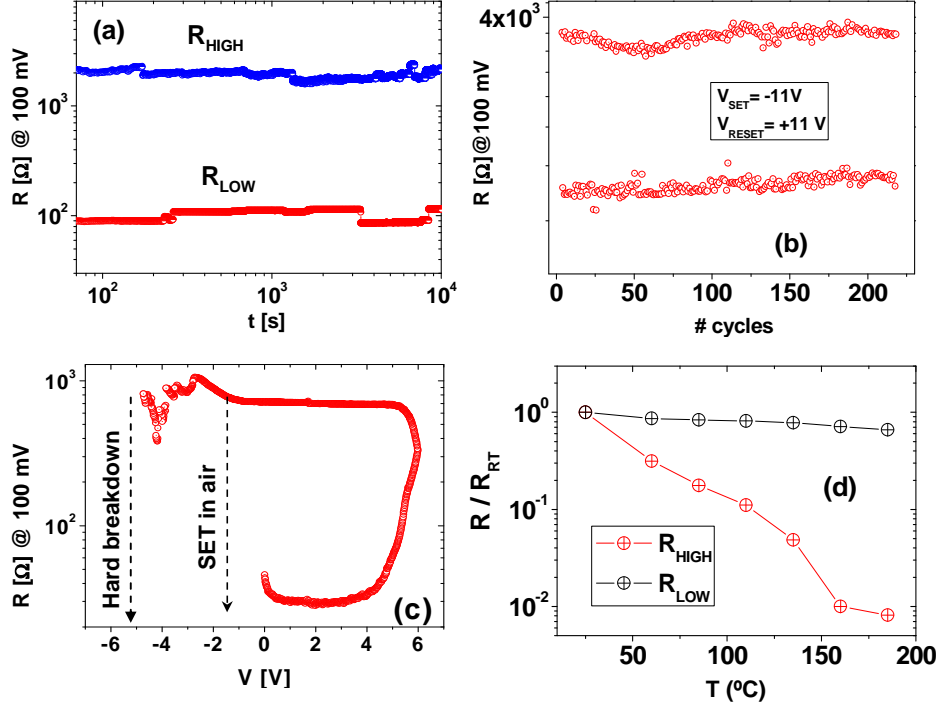


Figure 2: (a) Retention experiments corresponding to a NSTO/LSMCO/Pt device, for both R_{LOW} and R_{HIGH} states; (b) Endurance test performed by applying single voltage pulses with opposite polarities ($\pm 11\text{V}$). A stable behavior is observed; (c) Vacuum hysteresis switching loop of a formed NSTO/LSMCO/Pt device. The RESET transition occurs at a voltage similar to devices measured in air, but the SET transition does not appear, indicating that this transition is linked to the absorption of environmental O_2 to oxidize the LSMCO. At $\sim -5\text{V}$ hard dielectric breakdown takes place and the resistance permanently drops to a few ohms; (4) Evolution of the remnant states R_{LOW} and R_{HIGH} as a function of the temperature. A semiconducting-like behavior is found for both states.

The experimental memristive behavior, characterized by the HSL (Figure 1(c)), was simulated by adapting the voltage enhance oxygen vacancies drift (VEOV) model,^[8,9,13] originally developed to describe oxygen vacancies electromigration for “closed” systems, to an “open” system that allows oxygen exchange with the environment. The simulation assumes a 1D chain of LSMCO nanodomains, able to accommodate different oxygen content which controls their

resistivity, in contact with an oxygen reservoir. Oxygen ions can drift-diffuse between the reservoir and LSMCO and also between neighbor LSMCO nanodomains, under the application of external electrical stress. The model simulates the oxygen dynamics related to the electrically induced LSMCO oxidation and reduction. Further details of the simulations can be found in the Supplementary Information. The simulated HSL is shown with a solid line in Figure 1(c) and matches perfectly the experimental curve, supporting the importance of the LSMCO topotactic redox capability in the memristive behavior.

3.2. Analysis of the electroforming process at the nanoscale

The forming process was further analyzed by Scanning Transmission Electron Microscopy (STEM) in high angular annular dark field detector (HAADF). Analysis of a pristine device shows a high-quality epitaxial structure, an atomically-sharp NSTO/LSMCO interface and confirms the absence of extended defects such as dislocations or stacking faults (Suppl. Figure S5). Energy-dispersive X-ray spectroscopy (EDX) quantification indicates an average LSMCO stoichiometry consistent with the oxidized phase.

After forming, a significant change in the LSMCO nanostructure is observed. Figure 3(a) shows the STEM-HAADF cross-section of a formed NSTO/LSMCO/Pt device. Both the Pt electrode and the LSMCO films appear re-crystallized in a central zone, corresponding to Zone 1 in Figure 1(d). The epitaxial LSMCO structure changes to a polycrystalline arrangement of perovskite non-epitaxial nanograins, as displayed in Figure 3(b). This re-crystallization process is likely driven by the presence of thermal self-accelerated effects^[28] that follow the soft electrical breakdown produced by the application of high electrical field during forming. In addition, some of the analyzed lamellas display the presence of empty “bubbles”, surrounded by amorphous LSMCO, at the boundary between Zones 1 and 2. This is shown in Figure 3(c) and supports an electroforming mechanism involving the release of O₂ gas from the lattice. The presence of zones with some expelled material in Zone 2 is confirmed by Figure 3(a). STEM-HAADF images of Zone 3 (Figure 1(d)), 10 μm away from the boundary with Zone 2, show the presence of epitaxial LSMCO, now with horizontally aligned extended defects such as dislocations and both stacking^[29] and Ruddlesden-Popper (RP) faults, absent in the pristine sample (see Figure 3(d) and Supp. Fig. S6). It is suggested that grain boundaries and extended defects form channels with high oxygen mobility, necessary for the reversible LSMCO redox process linked to the memristive behavior.

Fast Fourier Transforms (FFT) performed on nanograins close to the LSMCO/NSTO interface (Zone 1) show that they remain structurally very similar to pristine LSMCO. In contrast, the

nanocrystals closest to the Pt top electrode exhibited extra diffraction spots attributed to the presence of long-range ordered oxygen vacancies (Figures 4(a)-(c)).

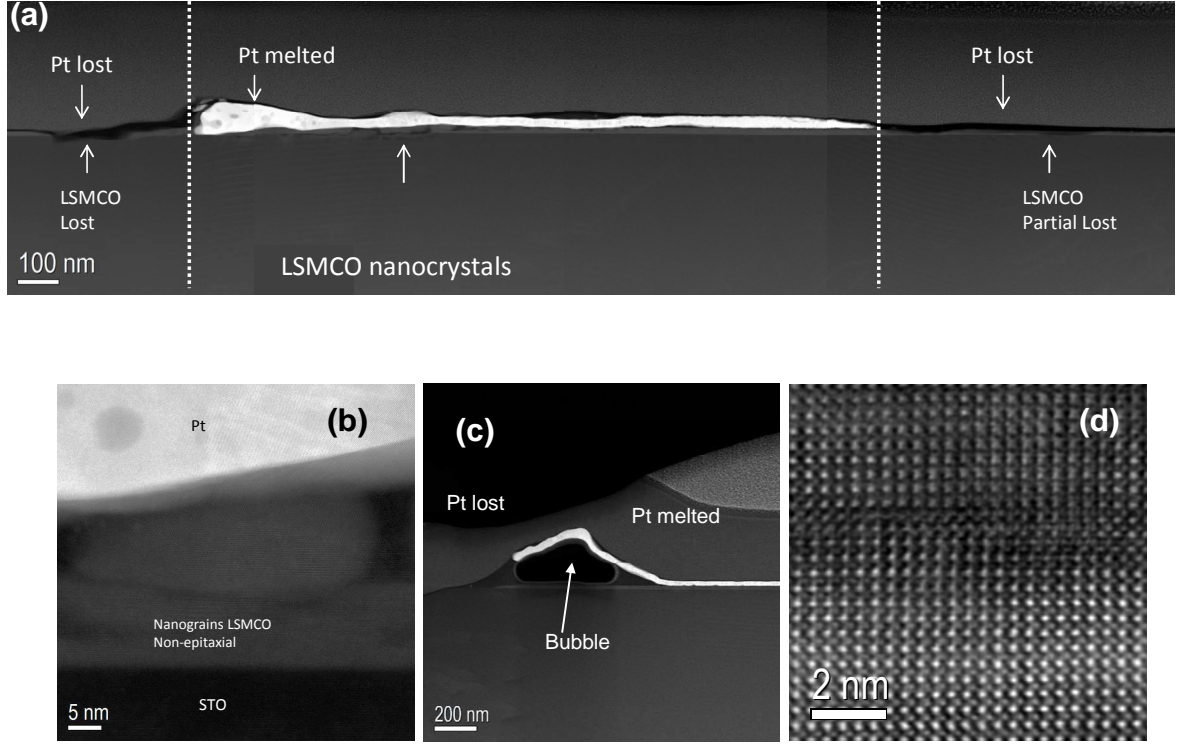


Figure 3: (a) Cross-section STEM-HAADF corresponding to a NSTO/LSMCO/Pt formed device. A central re-crystallized zone is seen (Zone 1), surrounded by a zone of expelled material (Zone 2); (b) Enlargement of the central zone, displaying the presence of non-epitaxial LSMCO nanograins; (c) Enlargement of the border between the re-crystallized and expelled zones, showing the presence of an empty “bubble”, indicating that oxygen gas is released during the forming process (note that this image is from a different lamella than that shown in Figure 3(a)); (d) High resolution STEM-HAADF cross-section of LSMCO at Zone 3, showing that epitaxy is preserved upon forming but extended defects are created.

This is confirmed by EELS/EDS compositional studies with O ~50-55 at%, which indicates oxygen depletion in those surface grains. Additionally, we observe variations in the cation stoichiometry in the direction perpendicular to the film surface. Figure 4(d) shows EELS profiles for La, Co, Mn, O and Ti, indicating that the nanograins close to the NSTO substrate present a stoichiometry similar to the pristine compound, but those close to the top Pt electrode have a depleted stoichiometry of Co, Mn and O. The different surface chemical phase prevents deeper LSMCO from spontaneous re-oxidation, improving the retentivity of the devices.

Figure 4(e) summarizes in a sketch the proposed forming and memristive mechanisms.

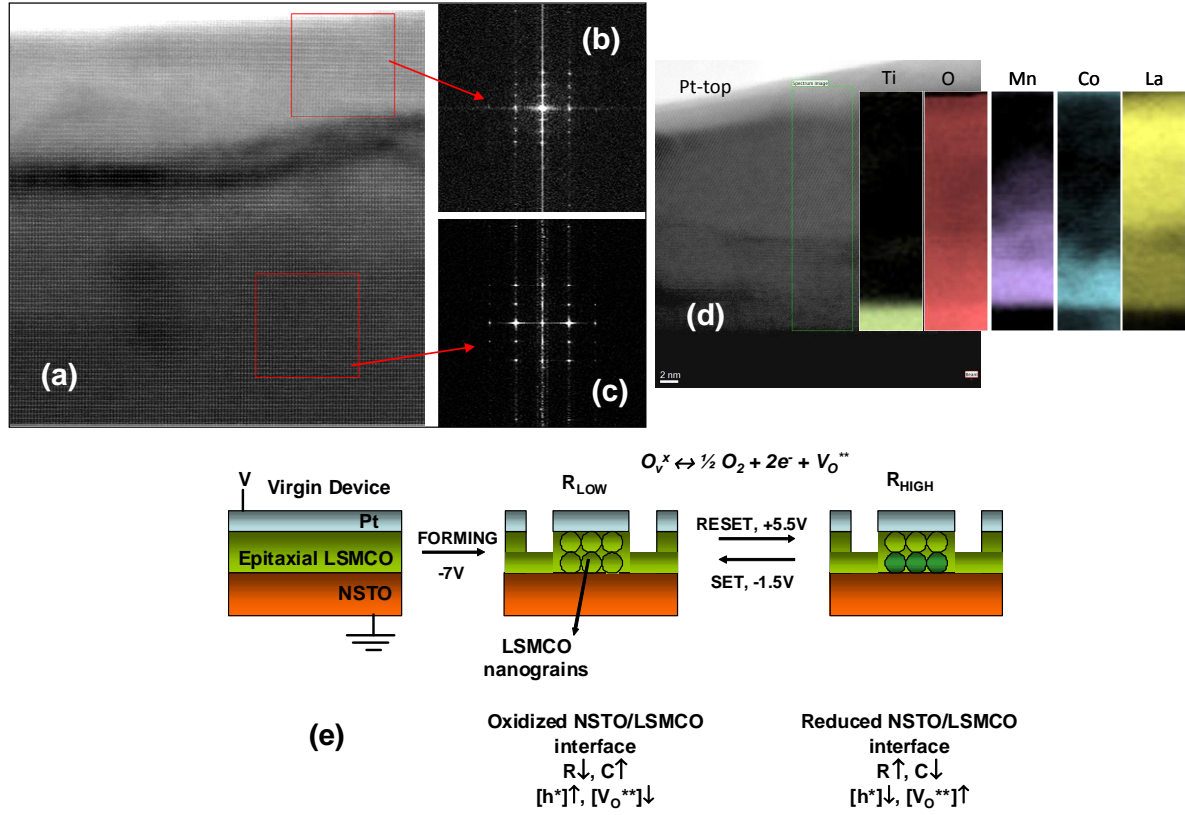


Figure 4: (a), (b), (c) Fast Fourier transforms (FFT) of STEM-HAADF images recorded in Zone 1. It is found that LSMCO nanograins near to the interface with NSTO present a perovskite structure similar to the pristine sample, while the grains in the upper part of the device, close to the Pt interface, have FFTs with extra reflections which can be attributed to the presence of ordered oxygen vacancies; (d) EELS line scans performed on the LSMCO nanograins in Zone 1 show that the upper grains (close to the interface with Pt) present a depleted stoichiometry of Mn, Co and O; (e) Sketch of the forming, RESET and SET processes in the NSTO/LSMCO/Pt devices. Structural modifications of the epitaxial LSMCO films are produced after forming. In Zone 1 (below the tip used for electrical contact with Pt), LSMCO is recrystallized and non-epitaxial nanograins are formed. Some material is expelled from Zone 2. LSMCO in Zone 3 (~10μm away from Zone 2) retains its epitaxial character but extended defects, absent in the pristine film, are formed. The transition between R_{LOW} and R_{HIGH} is related to the oxidation and reduction of the NSTO/LSMCO interface.

3.3. Understanding the memristive and memcapacitive mechanisms

To obtain further insight into the proposed memristive mechanism, we analyzed the dynamic I-V curves corresponding to the two resistive states by plotting the power exponent $\gamma =$

$d(\ln(I))/d\ln(V)$ as a function of $V^{1/2}$.^[30] It has been shown^[31-33] that this method is useful for identifying the presence of multiple conduction mechanisms, which often occur in metal/complex oxide interfaces.^[34,35] Figure 5(a) shows the complex evolution of γ vs. $V^{1/2}$ for both R_{HIGH} and R_{LOW} , indicating the presence of several circuit elements with relative weights that change between R_{HIGH} and R_{LOW} .

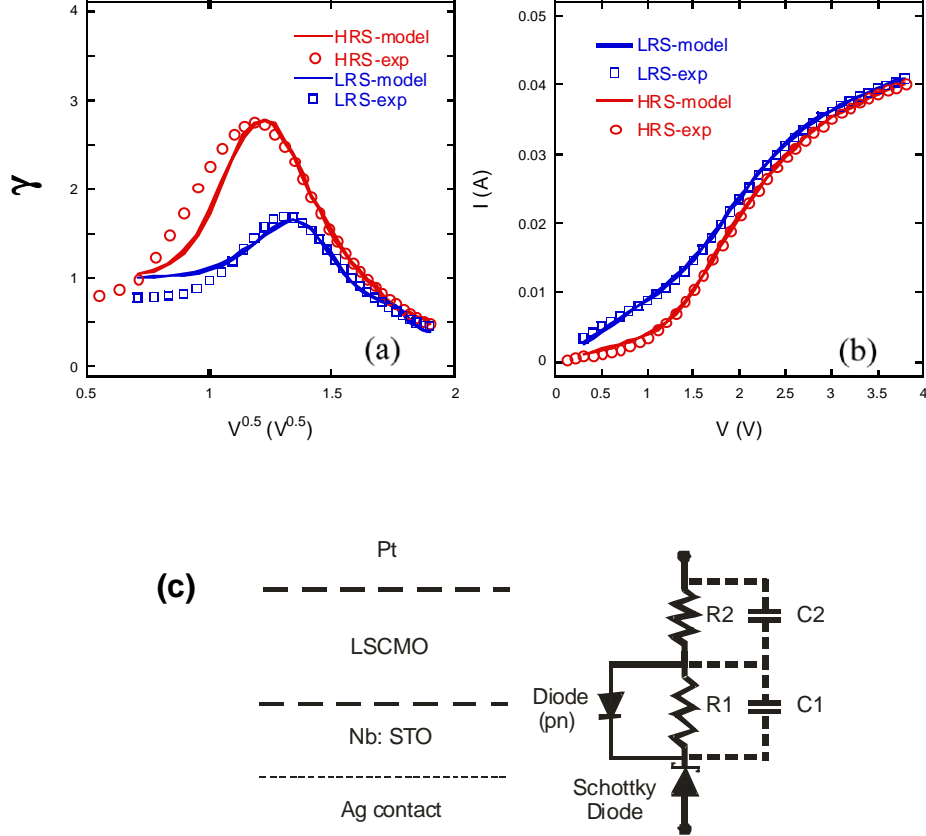


Figure 5: (a) γ vs. $V^{1/2}$ representation and (b) corresponding I-V curves for both the experimental (open symbols) and the calculated (solid line) R_{HIGH} and R_{LOW} states. The fits are performed by considering the equations derived from the proposed equivalent circuit presented in (c). For completeness, we have included the capacitors associated with each interfacial region in the equivalent circuit (dotted lines), however they can be disregarded for the I-V modeling as the characteristic times involved in these measurements are sufficiently long (~ 1 ms) to consider them in a steady state condition

The equivalent circuit that correctly describes the γ vs. $V^{1/2}$ behavior is shown in Figure 5(c) and includes the series combination of: i) an n-p diode in parallel with a leakage channel, corresponding to the NSTO/ LSMCO interface and characterized by the diode inverse saturation I_{satpn} and real thermal voltage V_{tpn} , and the parallel resistor R_1 , ii) the series resistor R_2 associated with the ohmic conduction of non-interfacial LSMCO plus the LSMCO/Pt interface, and iii) a

Schottky diode linked to the external Ag/NSTO contact, characterized by the parameters I_{satsch} and V_{tsch} . The experimental I-V curves were fitted by numerically solving the implicit I-V equations of the circuit, and all circuit parameters were extracted and listed in Table 1. Further details of this procedure can be found on the Supplementary Information. Figure 5(b) shows the excellent fits of the experimental I-V curves for both R_{HIGH} and R_{LOW} states. The quality of the fits can also be seen in the γ vs. $V^{1/2}$ curves (see Figure 5(a)) where their shape is well described, besides small deviations at low voltages attributed to the presence of small thermoelectric voltages. The fittings indicate that the transition between R_{HIGH} and R_{LOW} is dominated by the metallization of the LSMCO/NSTO interface, reflected in the increase of the n-p diode inverse saturation I_{satpn} and the decrease of the leakage resistance R_l . A reduction of the R_2 resistance is also observed, indicating the creation of a conducting channel through LSMCO, with a small contribution to the overall resistance change. As expected, the Ag/NSTO Schottky diode parameters remain unchanged.

	$R_1 [\Omega]$	$R_2 [\Omega]$	$V_{tpn} [V]$	$I_{satpn} [\mu A]$	$V_{tsch} [V]$	$I_{satsch} [mA]$
R_{HIGH}	270	23	0.15	2.5	0.60	51
R_{LOW}	110	1	0.24	5.6	0.57	50

Table 1: Fitting parameters for the I-V curves obtained after numerically solving the I-V relationship (see Supplementary Information) derived from the equivalent circuit model shown in Figure 5(c), both for R_{HIGH} and R_{LOW} states. The majority of the memristive change can be attributed to the metallization of the LSMCO/NSTO interface. The uncertainties of the fitted parameters are around 10 %.

Impedance spectroscopy was performed to further investigate the memristive mechanism, and Figures 6(a) and (b) display the Cole-Cole plots for both R_{HIGH} and R_{LOW} respectively. While R_{LOW} shows a full semicircle, only a partial semicircle is recorded for R_{HIGH} . The equivalent circuit that allows a good fit of the R_{LOW} state is shown in Figure 6(e). The same equivalent circuit was used to simulate the R_{HIGH} spectrum. The fitted values for the circuit elements are shown in Table 2. We attribute the R_3^*/C_3^* elements to the LSMCO/Pt interface, R_1^*/C_1^* to the NSTO/LSMCO interface, and the series resistance R_2^* includes the non-interfacial LSMCO plus the contribution of the Ag/NSTO interface. We note that R_2 in Figure 5(c) includes both R_2^* and R_3^* of the AC equivalent circuit of Figure 6(e) and that the n-p diode AC contribution is included in R_l^* . It is observed that R_3^* does not significantly change between R_{HIGH} and R_{LOW} ,

confirming that LSMCO/Pt is a non-memristive interface. In contrast, the NSTO/LSMCO interface substantially changes its resistance between R_{LOW} and R_{HIGH} , as R_1^* goes from $\sim 10\ \Omega$ to $\sim 500\ \Omega$, respectively. Concurrently, R_2^* displays a smaller change between $\sim 20\ \Omega$ and $\sim 90\ \Omega$ due to the reduction of the LSMCO lattice that leads to a decrease of holes for the p-type conduction. These results confirm that the memristive behavior is dominated by changes at the diode interface.

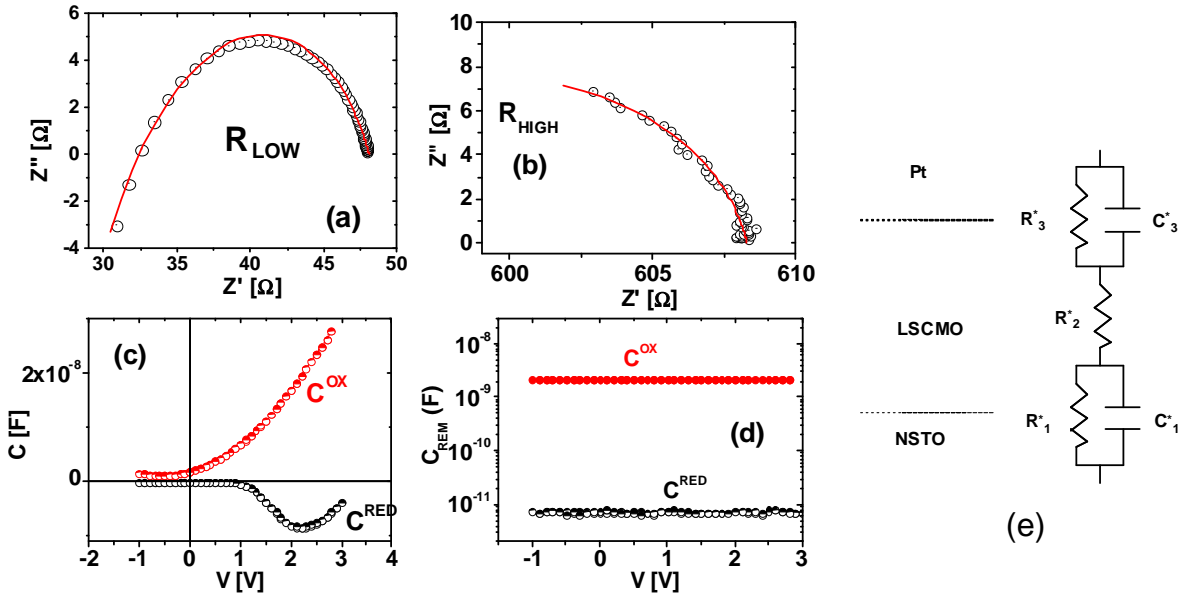


Figure 6: (a), (b) Impedance spectroscopy spectra recorded for both R_{LOW} and R_{HIGH} states respectively. The experimental points are shown with open symbols, while the fittings are shown with solid lines; (c), (d) Dynamic and remnant capacitance-voltage (C-V) curves recorded both for the oxidized (corresponding to R_{LOW}) and reduced (corresponding to R_{HIGH}) LSMCO states. The stimuli protocols are described in the Experimental section; (e) Equivalent AC circuit proposed to model the experimental impedance spectroscopy data.

The topotactic redox process occurring at the interface leads to remarkable behavior due to the biggest memcapacitive response reported to date.^[17-23] While the capacitance C_3^* of the LSMCO/Pt interface ($\sim 10^{-9}$ F) displays a marginal change during switching, we observe a large change in the diode capacitance C_1^* , from $C_1^{OX} \sim 3 \times 10^{-8}$ F for R_{LOW} to $C_1^{RED} \sim 1 \times 10^{-12}$ F for R_{HIGH} , which is a giant memcapacitive effect with a C_1^{OX}/C_1^{RED} ratio of $\sim 10^4$. The impact of the C_1^* variation on the overall capacitance of the device (LSMCO/Pt interface in series with the diode interface), was determined with dynamic and remnant C-V curves on devices prepared in both R_{HIGH} and R_{LOW} states (Figures 6(c) and (d)). A significant difference in the dynamic C-V curves between C^{OX} and C^{RED} states is observed. The negative capacitance found for C^{RED} for

positive voltages is attributed to the non-monotonic or positive-valued behaviour of the time-derivative of the transient current in response to a small voltage step.^[36] The remnant measurements values for C^{OX} and C^{RED} , of 2×10^{-9} F and 6×10^{-12} F respectively, demonstrates the ability of this device to reversibly change its capacitance between two non-volatile states with a C^{OX}/C^{RED} ratio > 300 . This is the largest figure measured to date by at least a factor of 30.^[17-23]

	$R_1^* [\Omega]$	$C_1^* [F]$	$R_2^* [\Omega]$	$R_3^* [\Omega]$	$C_3^* [F]$
R_{HIGH}	500	1.5E-12	90	18	5.9E-9
R_{LOW}	10	34E-9	17	21	2.9E-9

Table 2: Fitting parameters obtained from modeling the impedance spectroscopy spectra of Figure 6, for both R_{HIGH} and R_{LOW} states, assuming the equivalent circuit displayed in the same figure. The NSTO/LSMCO interface (diode) displays both memristive and memcapacitive effects. The uncertainties of the fitted parameters are around 10 %.

The donors density N_D^{NSTO} at Nb:STO (0.5wt%) is $\sim 5 \times 10^{18} \text{ cm}^{-3}$,^[37] while the acceptors density N_A^{OX} for the oxidized phase, assuming ~ 0.5 holes/f.u., is $\sim 1 \times 10^{22} \text{ cm}^{-3}$. This value is in agreement with N_A values reported for La-Ca and La-Sr manganites.^[38] From the latter we have $N_A^{OX} \gg N_D^{NSTO}$ for the oxidized junction, indicating that the diode depletion layer is localized at NSTO, giving the following expression for the junction capacitance per unit area C_j^{OX} :

$$C_j^{OX} = \epsilon_{NSTO} \left[\frac{q}{2\epsilon_{NSTO}(V_0^{OX} - V)} \frac{N_D^{NSTO} N_A^{OX}}{N_D^{NSTO} + N_A^{OX}} \right]^{1/2} \approx \left(\frac{\epsilon_{NSTO} q N_D^{NSTO}}{2(V_0^{OX} - V)} \right)^{1/2} \quad (1)$$

where q is the electronic charge, V_0^{OX} is the oxidized diode built-in potential, V is the applied bias and ϵ_{NSTO} is the NSTO permittivity. For the reduced phase ($\delta \sim 0.6$), each oxygen vacancy leaves two electrons behind (1.2 electrons/f.u.). Some of these electrons, with density N_D^{OV} , will recombine with holes and the rest will remain localized.^[39] We notice that $N_D^{OV} \sim N_A^{OX}$ and therefore the acceptor density for the reduced phase, given by $N_A^{RED} = N_A^{OX} - N_D^{OV}$, should be drastically reduced with respect to N_A^{OX} . If we assume that $N_A^{RED} \ll N_D^{NSTO}$, the reduced junction depletion layer would be localized at LSMCO, with the junction capacitance per unit area C_j^{RED} given by:

$$C_j^{RED} \approx \left(\frac{\epsilon_{LSMCO} q N_A^{RED}}{2(V_0^{RED} - V)} \right)^{1/2} \quad (2)$$

where ϵ_{LSMCO} and V_0^{RED} are the LSMCO permittivity and the built-in potential of the reduced junction. If we divide both sides of equations (1) and (2) and neglect differences between V_0^{OX} and V_0^{RED} and between ϵ_{NSTO} and ϵ_{LSMCO} , we get $C_j^{OX}/C_j^{RED} \sim (N_A^{OX}/N_A^{RED})^{1/2}$. From this relation, a value of $C_j^{OX}/C_j^{RED} \sim 10^4$ (as the obtained C_I^{OX}/C_I^{RED} ratio from IS) implies, as a rough estimation, that $N_A^{RED} \sim 10^{10} \text{ cm}^{-3}$, consistently with our previous assumption of $N_A^{RED} \ll N_A^{OX}$, N_D^{NSTO} . We therefore correlate the giant capacitance change at the diode with the topotactic redox ability of LSMCO, which allows large changes of the number of LSMCO charge carriers at the interface with NSTO.

4. Conclusions

Based on our measurements and observations, we propose the following scenario for the electrical behavior of NSTO/LSMCO/Pt devices. Upon the application of negative stimulus to the top Pt electrode, electrical current flows through a highly resistive path until soft-dielectric breakdown takes place via the formation of extended defects. Heating effects activate a self-accelerated re-crystallization process at the LSCMO layer below the landing zone of the electrical tip contacting Pt, where most of the electrical current is concentrated. Upon forming, LSCMO nanograins are formed, O_2 is released and some material is expelled from the area around this central zone. The *in situ* creation of nanograin boundaries and extended defects allows the post-forming easy migration of oxygen into and out of the device. Our characterization indicates that memresistance and memcapacitance take place at the NSTO/LSMCO interface, where a switchable n-p diode is formed. An oxidized interface leads to a R_{LOW} state with a thinner depletion layer and larger capacitance, and a reduced interface results in a R_{HIGH} state with thicker depletion layer and lower capacitance. The key factor for this behavior is the topotactic redox ability of LSMCO, which tolerates large changes in the donor/acceptor balance at the diode interface, due to the substantial difference in oxygen content between oxidized and reduced LSMCO phases. The giant memcapacitance measured on our devices is $\sim 2900\%$ larger than all similar effects reported to date, proving the potential of multi-mem interfaces based on topotactic redox oxides for disruptive neuromorphic computing devices.

Acknowledgements

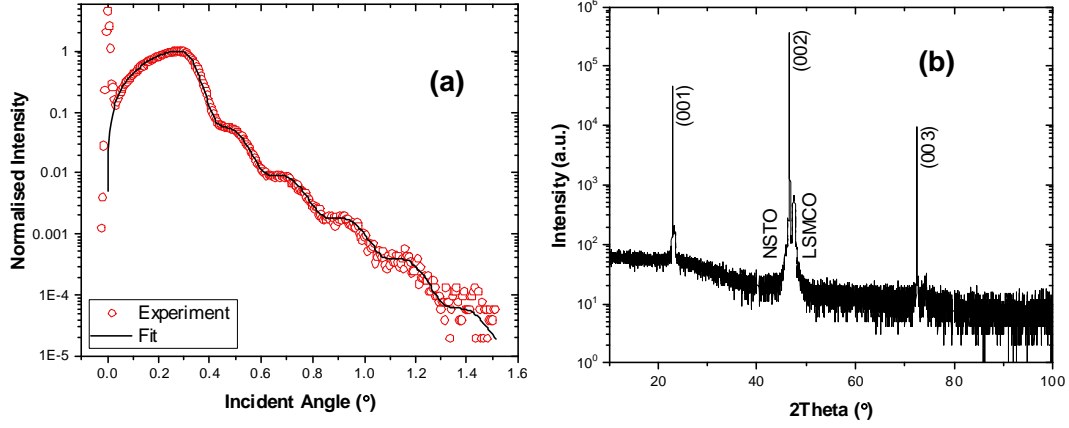
D.R. acknowledges financial support from ANPCyT, projects PICTs 0867 and 1836. Helpful discussions with S. Menzel, P. Stoliar, M. Rozenberg and P. Levy are acknowledged. We thank F. Golmar and L. Malatto, from INTI, for the access to the thermal probe station and FIB facility. A.A., C.vdB. and A.C. acknowledge the support of the Engineering and Physical Sciences Research Council (EPSRC), Grants No. EP/M014142/1, EP/P026478/1 and EP/L504786/1. M.A. also acknowledges financial support of H2020-MSCA-RISE-2016 SPICOLOST Grant No. 734187 to perform TEM studies at LMA-INA, University of Zaragoza.

References

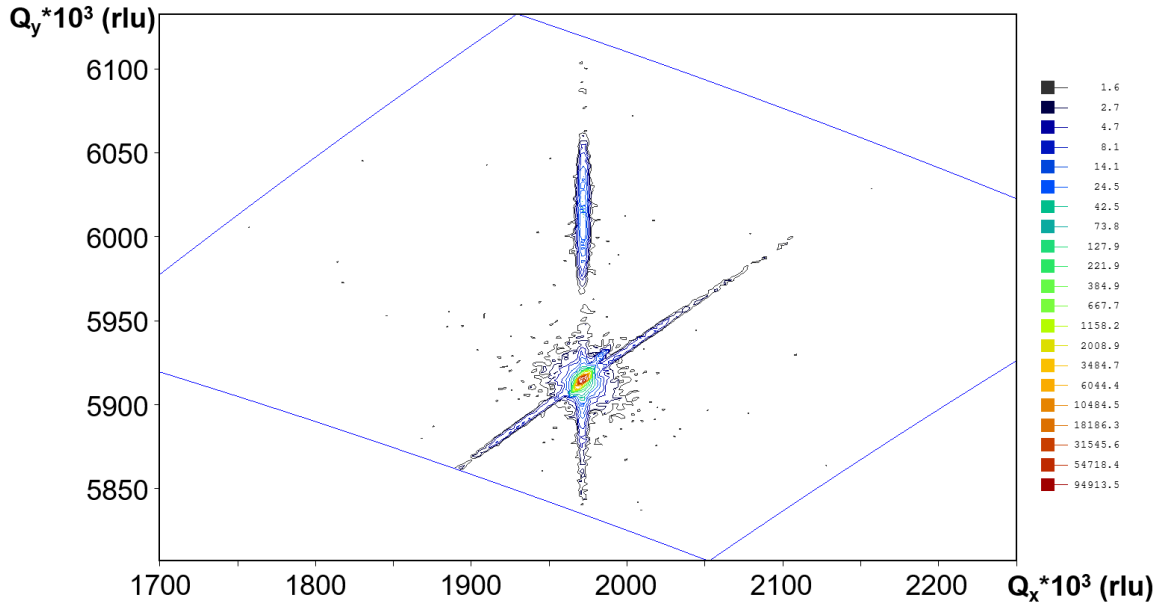
- [1] S. Yu, *Neuro-inspired computing using resistive synaptic devices*, Springer International Publishing, 2017
- [2] D. Ielmini, R. Waser, *Resistive Switching From Fundamentals of Nanoionic Redox Processes to Memristive Device Applications*, Wiley-VCH, 2016
- [3] Z. Wang, S. Joshi, S. E. Savel'ev, H. Jiang, R. Midya, P. Lin, M. Hu, N. Ge, J. P. Strachan, Z. Li, Q. Wu, M. Barnell, G. L. Li, H. L. Xin, R. S. Williams, Q. Xia, J. J. Yang, *Nat. Mater.* **16**, 101 (2017)
- [4] A. Sawa, *Mater. Today* **11**, 28 (2008)
- [5] R. Waser, R. Dittmann, G. Staikov, K. Szot, *Adv. Mater.* **21**, 2632 (2009)
- [6] J. Borghetti, G. S. Snider, P. J. Kuekes, J. J. Yang, D. R. Stewart, R. S. Williams, *Nature* **464**, 873 (2010)
- [7] S. Q. Liu, N. J. Wu, A. Ignatiev, *Appl. Phys. Lett.* **76**, 2749 (2000)
- [8] M. J. Rozenberg, I. H. Inoue, M. J. Sánchez, *Phys. Rev. Lett.* **92**, 178302 (2004)
- [9] M. J. Rozenberg, M. J. Sánchez, R. Weht, C. Acha, F. Gomez-Marlasca, P. Levy, *Phys. Rev. B* **81**, 115101 (2010)
- [10] D. Rubi, F. Tesler, I. Alposta, A. Kalstein, N. Ghenzi, F. Gomez-Marlasca, M. Rozenberg, P. Levy, *Appl. Phys. Lett.* **103**, 163506 (2013)
- [11] A. Herpers, C. Lenser, C. Park, F. Offi, F. Borgatti, G. Panaccione, S. Menzel, R. Waser, R. Dittmann, *Adv. Mater.* **26**, 2730 (2014)
- [12] S. Asanuma, H. Akoh, H. Yamada, A. Sawa, *Phys. Rev. B* **80**, 235113 (2009)
- [13] W. Román Acevedo, C. Ferreyra, M. J. Sánchez, C. Acha, R. Gay, D. Rubi, *J. Phys. D: Appl. Phys.* **51**, 125304 (2018)
- [14] A. Nemudry, E. Goldberg, M. Aguirre, M. Alario-Franco, *Solid State Sci.* **4**, 677 (2002)
- [15] A. Aguadero, H. Falcon, J. M. Campos - Martin, S. M. Al - Zahrani, J. L. G. Fierro, J. A. Alonso, *Angew. Chem. Int. Ed.* **50**, 6557 (2011)
- [16] V. R. Nallagatla, J. Jo, S. K. Acharya, M. Kim, C. U. Jung, *Sci. Rep.* **9**, 1188 (2019)
- [17] I. Salaoru, A. Khiat, Q. Li, R. Berdan, T. Prodromakis, *Appl. Phys. Lett.* **103**, 233513 (2013)
- [18] S. X. Wu, H. Y. Peng, T. Wu, *Appl. Phys. Lett.* **98**, 093503 (2011)
- [19] A. A. Bessonov, M. N. Kirikova, D. I. Petukhov, M. Allen, T. Ryhänen, M. J. Bailey, *Nat. Mater.* **14**, 199 (2015)
- [20] I. Salaoru, Q. Li, A. Khiat, T. Prodromakis, *Nanoscale Res. Lett.* **9**, 552 (2014)
- [21] P. Yang, H. Jun Kim, H. Zheng, G. Won Beom, J. S. Park, C. Jung Kang, T. S. Yoon, *Nanotechnology* **28**, 225201 (2017)
- [22] D. Park, P. Yang, H. J. Kim, K. Beom, H. H. Lee, C. J. Kang, T. S. Yoon, *Appl. Phys. Lett.* **113**, 162102 (2018)
- [23] R. Liu, R. Dong, X. Yan, S. Yuan, D. Zhang, B. Yang, X. Xiao, *Appl. Phys. Express* **11**, 114103 (2018)
- [24] D. Tran, C. Teuscher, <https://arXiv.org/abs/1704.05921> (2017)
- [25] L. Nielen, A. Siemon, S. Tappertzhofen, R. Waser, S. Menzel, E. Linn, *IEEE J. Emerg. Sel. Topics Circuits Syst.* **5**, 153 (2015)
- [26] A. Herpers, *Electrical characterization of manganite and titanate structures*, PhD Thesis, Forschungszentrum Jülich, 2014
- [27] J. Joshua Yang, Feng Miao, Matthew D. Pickett, Douglas A. A. Ohlberg, Duncan R. Stewart, Chun Ning Lau, R. Stanley Williams, *Nanotechnology* **20**, 215201 (2009)
- [28] U. Russo, D. Ielmini, C. Cagli, A. L. Lacaita, *IEEE Trans. Electron Dev.* **56**, 193 (2009)
- [29] Andrey Shkabko, Myriam H. Aguirre, Amit Kumar, Yunseok Kim, Stephen Jesse, Rainer Waser, Sergei V. Kalinin, Anke Weidenkaff, *Nanotechnology* **24**, 475701 (2013)
- [30] C. Acha, *J. Appl. Phys.* **121**, 134502 (2017)
- [31] C. Acha, A. Schulman, M. Boudard, K. Daoudi, T. Tsuchiya, *Appl. Phys. Lett.* **109**, 11603 (2016)

- [32] W. R. Acevedo, C. Acha, M. J. Sánchez, P. Levy, D. Rubi, *Appl. Phys. Lett.* **110**, 053501 (2017)
- [33] N. Ghenzi, M. Barella, D. Rubi, C. Acha, *J. Phys. D: Appl. Phys.* **52**, 125401 (2019)
- [34] B. Ghosh, K. Das, A. K. Raychaudhuri, *J. Appl. Phys.* **109**, 083934 (2011)
- [35] F. Gomez-Marlasca, N. Ghenzi, A. G. Leyva, C. Albornoz, D. Rubi, P. Stoliar, P. Levy, *J. Appl. Phys.* **113**, 144510 (2013)
- [36] M. Ershov, H.C. Liu, L. Li, M. Buchanan, Z.R. Wasilewski, A.K. Jonscher, *IEEE Trans. Electron Dev.* **45**, 2196 (1998)
- [37] K. Ozdogan, M. U. Kahaly, S. R. S. Kumar, H. N. Alshareef, U. Schwingenschlögl, *J. Appl. Phys.* **111**, 054313 (2012)
- [38] I. M. Dildar, C. Beekman, X. He, J. Aarts, *Phys. Rev. B* **85**, 205103 (2012)
- [39] Kitae Eom, Euiyoung Choi, Minsu Choi, Seungwu Han, Hua Zhou, Jaichan Lee, *J. Phys. Chem. Lett.* **8**, 3500 (2017)

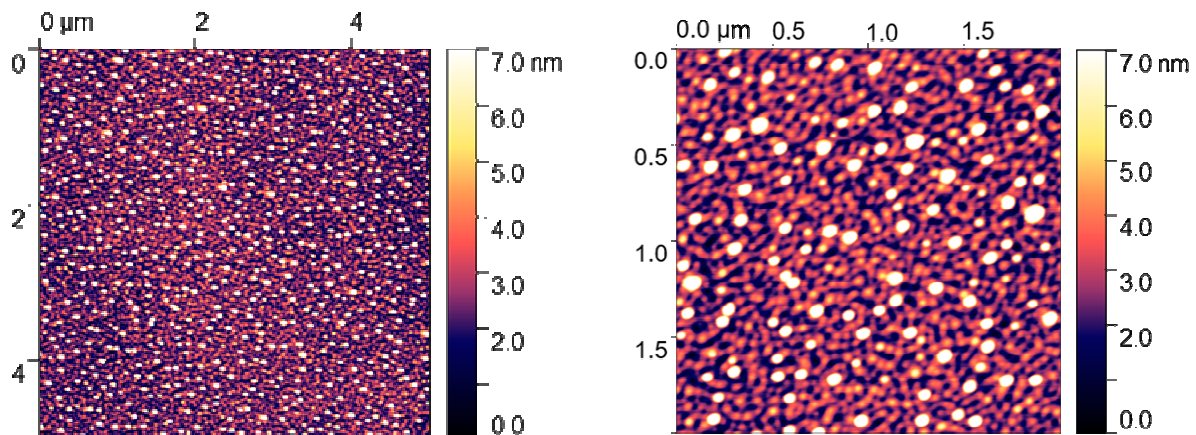
Supplementary material



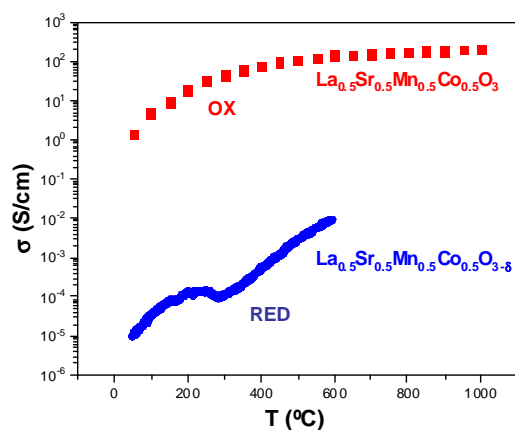
Supplementary Figure S1: (a) X-ray reflectivity measurement of as-grown LSCMO/NSTO. A thin film thickness of $\sim 20\text{nm}$ was extracted by modeling the experimental data; (b) Bragg-Brentano X-ray diffraction pattern of as-grown epitaxial LSMCO/NSTO showing only (00l) diffraction peaks.



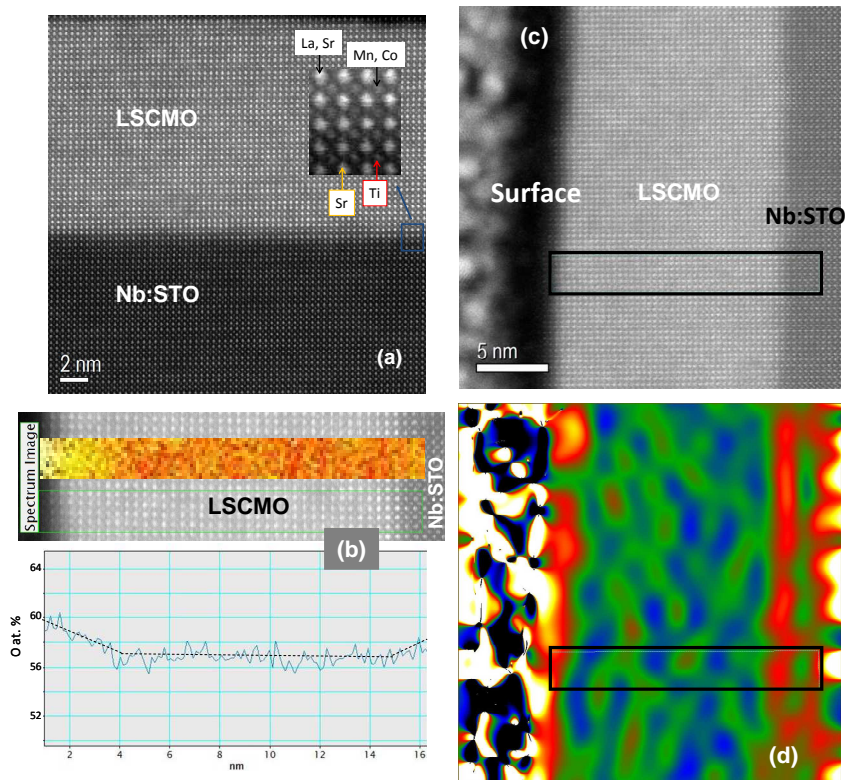
Supplementary Figure S2: X-ray reciprocal space map recorded for an as-grown LSCMO thin film around the non-specular (103) reflection. This confirms the thin films are fully strained, as the reflections of both the substrate and the film are aligned in Q_x , the in-plane (parallel) projection of the reciprocal lattice vector.



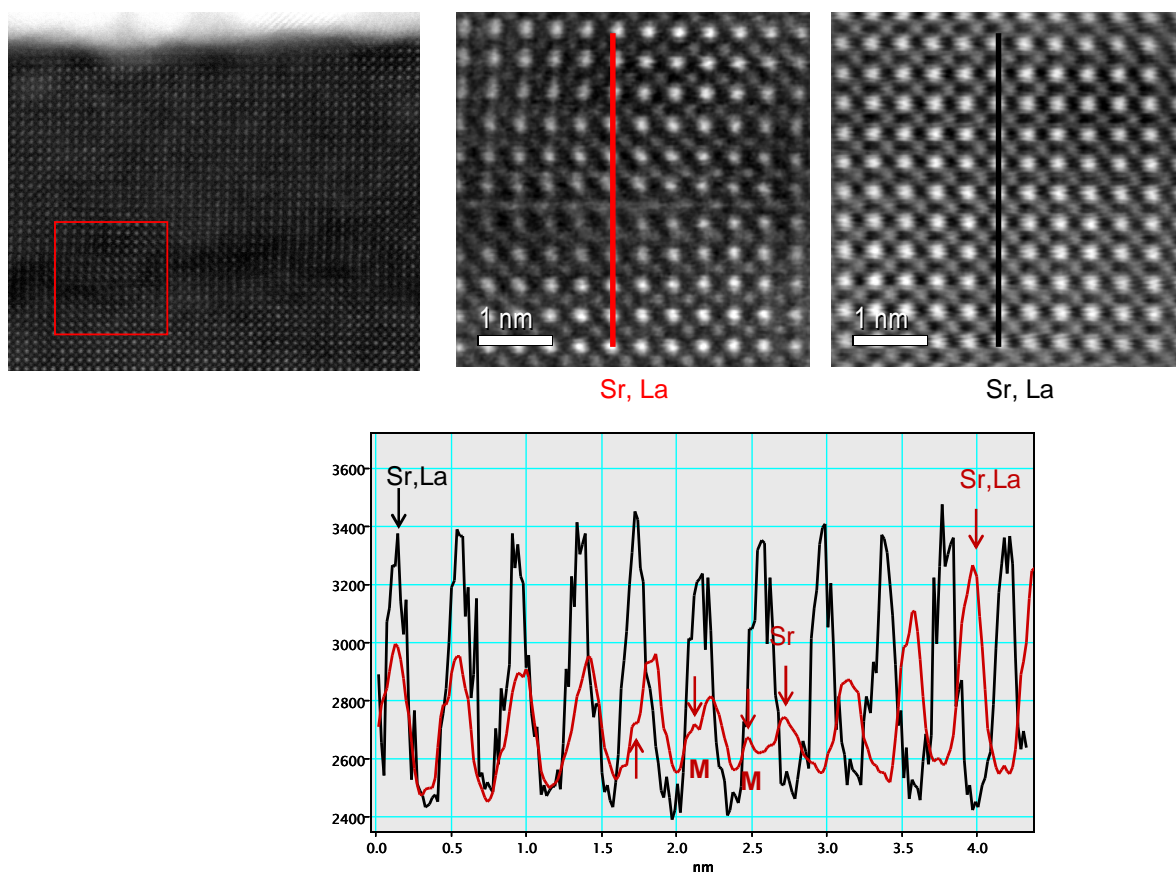
Supplementary Figure S3: Atomic force microscopy images (5×5 and $2 \times 2 \mu\text{m}^2$ scans) corresponding to an as-grown LSCMO thin film. The root mean square (RMS) roughness was estimated in 2.7 nm.



Supplementary Figure S4: 4-points conductivity as a function of the temperature for bulk (ceramic) oxidized and reduced LSCMO. Conductivity values of the reduced phase might be underestimated due to the formation of cracks during the reducing annealing.



Supplementary Figure S5: (a) STEM-HAADF image of a pristine NSTO/LSCMO thin film. The presence of a well defined, sharp interface is evident; (b-up) Electron energy loss spectroscopy (EELS) line-scan measured on the same sample; (b-low) Oxygen quantification obtained from an electron energy loss spectroscopy (EELS) line scan, indicating a relative slight oxygen excess in the LSCMO zone close to both the interface with the NSTO substrate and the surface. This correlates with the geometrical phase analysis (GPA) of the HAADF images, shown in (c) and (d), which show the presence of negative strain in LSCMO respect to the STO cell in the central part of the film ($E_{yy} < 0$), while there is a small cell dilatation (positive strain, $E_{yy} > 0$) on both the interface with NSTO and the surface.



Supplementary Figure S6: Defect analysis, showing the shift of La-Sr and Mn-Co (M) columns. Red line corresponds to atomic intensity of a defective column and black line to atomic intensity of a non-defective column. In the analysis metals appear near the same column of La-Sr (when originally have to be $\frac{1}{2}$ unit cell displaced) and La-Sr shift $\frac{1}{2}$ unit cell in a mixed stacking fault and RP defect. These defects are likely at the origin of cracks and material ejection after electroforming.

Hysteresis Switching Loop simulation

To simulate the experimental hysteresis switching loops (HSL), linked to the $\text{La}_{0.5}\text{Sr}_{0.5}\text{Mn}_{0.5}\text{Co}_{0.5}\text{O}_{3-\delta}$ (LSCMO) topotactic redox ability, we have assumed a 1D chain of LSCMO nanodomains, able to oxidize and reduce by capturing or releasing oxygen ions. The domain located at one extreme of the chain is in contact with an oxygen reservoir, which can inject or remove oxygen ions from the LSCMO nanodomains chain. Oxygen ions are also able to electromigrate between adjacent LSCMO nanodomains.

For each LSCMO domain, we propose a simple linear relation between the local oxygen vacancies concentration and its resistivity (see Refs. [9, 13] in the main text):

$$\rho_i = A_i \eta_i$$

where A_i is a proportionality factor, taking values $\sim 6-8$ a.u.. A completely oxidized (reduced) nanodomain will present $\eta_i^{\text{MIN}} \sim 2 \times 10^{-5}$ a.u. ($\eta_i^{\text{MAX}} \sim 1 \times 10^{-4}$ a.u.).

The probability of migration from domain i to a nearest- neighbor site j is:

$$p_{ij} = \eta_i (1 - \eta_j) \exp(-V_0 + \Delta V_i)$$

where V_0 is the activation energy for vacancies diffusion and ΔV_i accounts for the voltage drop at each domain linked to the applied external stimuli.

We compute $\Delta V_i = V_{i+1} - V_i$ with the local voltage $V_i = I \rho_i$.

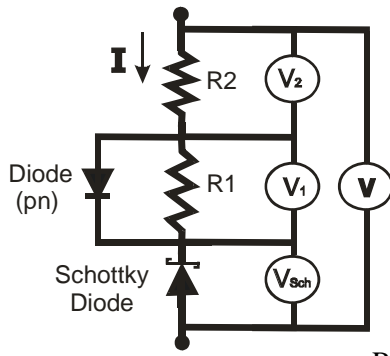
At each simulation time step, a given external voltage $V(t)$ is applied to the resistive chain. The current through the system is computed as $I(t) = V(t)/R$, with R being the series combination of all nanodomains resistivities.

Note that in the experimental HSL (Figure 1(c)), there are marked changes in the rate of the resistive change during both RESET and SET. The RESET process happens in two-steps, each of them presenting a steep resistance increase. The SET process is softer, but there is still a noticeable change in the resistance change velocity above certain voltage threshold. This is an indication of complex reaction kinetics. These features could be reproduced in the simulation by allowing an increase of the LSCMO activation energies (from $V_0 = 19$ a.u. to $V_0 = 28$ a.u.) above certain vacancies concentration thresholds. Under this assumption, the simulated HSL corresponds well with the experimental one.

I-V curves modeling

A proper way to graphically analyze the I-V curves consists of plotting the power exponent $\gamma = d(\ln(I))/d\ln(V)$ vs. $V^{1/2}$. This method is particularly useful for systems presenting coexisting conducting mechanisms, represented by complex equivalent circuits [28-30]. From Figure 5(a), it is found that for both R_{HIGH} and R_{LOW} γ is initially close to 1 for small voltages (ohmic behavior, parallel resistor), increases with a quadratic-like shape (n-p diode) and displays a cusp for higher voltages, indicating the presence of a current-limiting circuit element (series resistor). The cusp is shifted to higher voltages and lower γ values for the R_{LOW} curve indicating the reduction of the non-linear behavior as a consequence of a conductivity increase of both ohmic elements. Finally, for the highest voltages explored, γ decreases monotonically to values close to 0 (i.e. to a voltage-independent current)

The equivalent circuit model that describes the electrical behavior is shown below, and is represented by the following equations:



$$V = V_{Sch} + V_1 + V_2 ,$$

with the Schottky diode in inverse,

$$I_{Sch} = I_{satSch} \left[1 - e^{-\left(\frac{V_{Sch}}{V_{tSch}}\right)^{1/2}} \right] \text{ and } V_2 = R_2 I$$

where $I_{satSch} = A^* T^2 e^{-\frac{\phi_B}{k_B T}}$ is the inverse saturation current of the Schottky diode (ϕ_B being the Schottky barrier, A^* the

Richardson constant), and $V_{tSch} = \frac{4\pi\epsilon d(k_B T)^2}{q^2}$, with ϵ the real part of

the static dielectric constant and d , a relevant distance where most of the voltage V_{tSch} drops.

As $I = I_{pn} + I_{R1} = I_{spn} \left\{ e^{\frac{V_1}{V_{tpn}}} - 1 \right\} + \frac{V_1}{R_1}$, then by replacing $V_2 = V - V_{Sch} - V_1$,

$$I = I_{satpn} \left\{ e^{\left[\frac{V - I R_2 - V_{tSch} \ln^2 \left(1 - \frac{I}{I_{satSch}} \right)}{V_{tpn}} \right]} - 1 \right\} + \frac{V - I R_2 - V_{tSch} \ln^2 \left(1 - \frac{I}{I_{satSch}} \right)}{R_1},$$

where I_{satpn} is the saturation current and V_{tpn} the thermal voltage of the p-n diode.

This implicit I-V relation is solved numerically in order to fit the experimental I-V curve by determining R_1 , R_2 , I_{satpn} , V_{tpn} , I_{satSch} and V_{tSch} . The interpretation of the fittings is discussed at the manuscript main text. It can be also mentioned that the obtained I_{satSch} (~ 50 mA) match very well with the calculated value for a Ag/NSTO Schottky diode of the experimental area of 1 mm^2 used for these contacts (considering a Richardson constant $A^* = 156 \text{ A cm}^{-2} \text{ K}^{-2}$; the work function of Ag, $W_{Ag} = 4.3 \text{ eV}$; and the electron affinity of NSTO, $X_{NSTO} = 3.9 \text{ eV}$).